Applications in Energy and Combustion Science 15 (2023) 100178

Contents lists available at ScienceDirect

Applications in Energy and Combustion Science

journal homepage: www.sciencedirect.com/journal/applications-in-energy-and-combustion-science

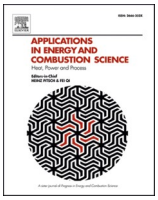

Deposition of graphenic nanomaterials from elevated temperature premixed stagnation flames

Shruthi Dasappa [1], Joaquin Camacho [*]

Mechanical Engineering Department, San Diego State University, San Diego, CA, USA 92110

ARTICLE INFO

Keywords:
Carbon nanoparticles
Graphenic carbon
HRTEM
XPS
Raman spectroscopy

ABSTRACT

The work examines the unique nanostructure of carbon nanoparticles deposited from sooting premixed flames with flame temperatures exceeding 2200 K. This flame temperature regime has previously been shown to transition from typical soot formation conditions to a regime whereby the flame-form carbon adopts a nanostructure considerably more ordered than soot. Graphenic carbon deposits observed by High-resolution TEM (HRTEM) are reported here corroborating previous Raman spectroscopy evidence. The use of premixed stretch-stabilized flames enables particle production in the high-temperature regime under a flow field amenable to low-dimensional flame modeling. Although the flame flow configuration is relatively simple, three sample preparation methods are used to assess the representation of true carbon properties as they exist in the flame. HRTEM imaging is carried out on carbon particle samples prepared by rapid-insertion deposition, aerosol dilution probe deposition and carbon particle film deposition. Images from rapid-insertion samples show amorphous particles in the lightly sooting flame and turbostratic particles in the heavy sooting flame. There is trace evidence of graphenic structure in rapid-insertion samples but the most striking particles on the TEM grid are graphite nanocrystals presumably formed by a new artificial crystallization process. HRTEM images of particles collected over time by diluted aerosol deposition and film deposition show clear graphenic structures. Overall, the carbon nanostructure observed by HRTEM is a mixture of amorphous, turbostratic and graphenic carbon lattices depending on the flame condition and sampling method. The current work highlights potential impacts of higher flame temperatures and higher equivalence ratio on deposited flame-formed carbon. Namely, graphenic particle structure is observed in rapid-insertion deposition samples but graphene portions are most abundant in aerosol dilution and carbon particle film deposition samples. This may indicate that graphene structures grow on the deposition surface over time.

Introduction

The formation of carbon particles in flames is unwanted during the energy conversion of fuel due to reduced performance [1] and problematic particulate emissions [2]. On the other hand, flame-formed carbon has always been a crucial source of light, heat and useful materials [3]. Gas-to-particle production of carbon black [4], fullerenes [5, 6] and graphenic materials [7] from hydrocarbon feedstocks have been shown to be a selective process that should be precisely controlled to avoid undesired soot formation. Transition metal catalysts have been used to guide the production of graphene in flames [8] and graphene production in flow reactors has been induced by microwave plasma [9, 10]. The current work examines carbon nanoparticles collected from premixed flames burning at temperatures exceeding 2200 K. Carbon particle films deposited from these flames were shown in previous work [11,12] to exhibit Raman spectra features much closer to graphenic materials than soot. These previous observations were explained by exceedingly high flame temperature which induce carbon lattice structures more crystalline than typical soot structure. The current work examines flame-formed carbon in this higher flame temperature regime with an emphasis on the potential selectivity towards graphenic structure depending on the sample collection method. Even higher flame temperatures and equivalence ratios are employed in the current work with the addition of particle characterization by high-resolution TEM and X-ray photoelectron spectroscopy (XPS).

The stretch-stabilized flame configuration used here is a steady

* Corresponding author.
E-mail address: jcamacho@sdsu.edu (J. Camacho).
[1] present address: Monolith, Lincoln, NE, USA 68508

https://doi.org/10.1016/j.jaecs.2023.100178
Received 17 April 2023; Received in revised form 12 July 2023; Accepted 13 July 2023
Available online 15 July 2023

axisymmetric laminar premixed flame with a relatively simple flow field and boundary conditions. Nonetheless, the interpretation of measurements obtained from flame-formed carbon warrants consideration of many potential sampling artifacts. Rapid-insertion deposition, particle film deposition and aerosol dilution probing are common ways to extract soot and flame formed carbon in experimental studies. Even in simple laboratory flames, however, the rapid insertion of a TEM sample grid is subject to artificial condensation [13] and exposure to many areas of the flame cross-section [14]. Films deposited from the flame are highly sensitive to the deposition conditions such as deposition time, flame composition and deposition surface temperature [11,15]. Aerosol probe sampling in flames requires careful optimization to quench reaction chemistry and avoid artificial aerosol growth processes [16,17]. Ideally, characterization of extracted flame particles would represent the nanostructure and composition as they develop in the flame. The experiments reported here will provide further insight into the formation of graphenic carbon in terms of the potential contribution of deposition processes and intrusive flame sampling.

Material and methods

The study is focused on flame-formed carbon in premixed stretch-stabilized flames (premixed stagnation flames) burning ethylene-oxygen-argon mixtures. These flames are stabilized by an aerodynamic balance rather than flame anchoring and this enables flame temperatures approaching the adiabatic flame temperature [18]. Under a suitable balance of convective velocity and flame speed, a steady flat flame could be established between the inlet nozzle and stagnation surface boundaries. An image of a typical sooting stretch-stabilized flame is shown is Fig. 1 along with images of the carbon particle films fabricated for the current work. Further details on the use of premixed stagnation flames under controlled flame temperature, equivalence ratio and particle growth time could be found elsewhere [19].

Two flame conditions are examined with flow rates and properties listed in Table 1. The flames are chosen here to have flame temperatures exceeding 2200 K with two different equivalence ratios, φ = 2.60 and 2.77. Soot yield is known to drop as temperatures exceed 2000 K as growth of PAH precursors becomes unfavored [20,21]. Our previous work on premixed stagnation flames showed the measured volume fraction decreased by 60% for a φ = 2.60 flame as the flame temperature increased from 2020 K to 2210 K [12]. The high equivalence ratio

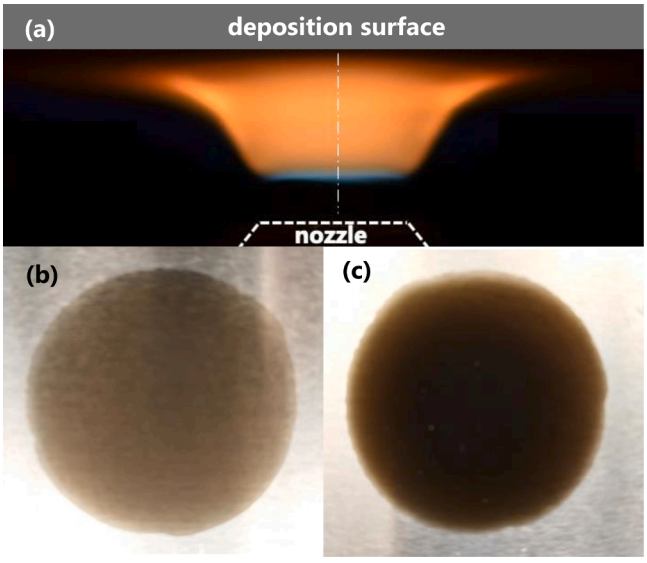

Fig. 1. Typical sooting stretch-stabilized flame (a), particle film deposited on the water-cooled, aluminum stagnation surface for the light sooting flame condition (Φ = 2.60, b) and heavy sooting flame condition (Φ = 2.77, c).

Table 1
Flame conditions and calculated global flame properties.

X_{C2H4}	X_{O2}	X_{Ar}	v_o (cm/s)	$T_{f,max}$ (K)	t_p (ms)	a (1/s)	T_{ad} (K)
ϕ = 2.6 flame							
0.223	0.258	0.518	92	2270	11	36	2199
ϕ = 2.77 flame							
0.260	0.282	0.457	81	2239	12	31	2150

required to form solid carbon at these temperatures introduces an abundance of carbon precursors in the post-flame region and this may affect the structure of carbon particle films deposited over time. In terms of nanostructure, we also reported that the Raman spectra of carbon films deposited on the stagnation surface deviate from typical soot Raman features as the flame temperature exceeded 2100 K [12]. This transition to graphene-like Raman spectra in the series of flames (6 flames spanning 1950 $K <$ Tflame $<$ 2250 K) was postulated to be caused by faster graphitization and crystallization of flame-formed carbon in this temperature range. The current study will examine three sample deposition methods discussed below to assess the selectivity towards graphenic nanostructure in the deposited carbon samples.

The reported flame temperature, $T_{f,max}$, is based on the flame structure computed by the CHEMKIN [22] OPPDIF [23] formulation of premixed stagnation flames [24]. Two-color pyrometry measurements previously reported by the authors [12] were shown to give a temperature profile consistent with the OPPDIF computations for a range of flame conditions. The computation incorporates temperatures at the nozzle and stagnation plate boundaries measured by type K thermocouple to be T_{nozzle} = 330 K and $T_{stagnation}$ = 400 K. USC Mech II [25] is used here as this model was previously shown to accurately capture the measured flame position [26]; a property very sensitive to chemical kinetics and gas-phase transport properties in premixed stagnation flames. The nozzle to stagnation plate separation distance is L = 2.54 cm for both flames. Based on the computed flame structure and thermophoretic velocity, the time it takes a particle to travel from the flame position to the stagnation plate is estimated to be t_p = 12 ms for both flame conditions. The global strain rate, a, is based on the cold gas velocity, v_o, and the separation distance. The adiabatic flame temperature is a constant pressure equilibrium solution. Further details on computational methods can be found elsewhere [19,24].

An experimental schematic highlighting the rapid-insertion deposition, aerosol dilution probe, and carbon particle film deposition sampling methods is shown in Fig. 2. Sampling of flame-formed carbon by rapid-insertion deposition is carried out by clamping a TEM grid (lacey carbon on copper, Ted Pella) onto a pneumatic cylinder. The cylinder pressure is controlled such the TEM grid penetrates the outer perimeter of the flame, dwells at the centerline and retracts in a fairly reproducible time. A single insertion is used for collection. Analysis of video frames indicates that the time the TEM grid is immersed in the flame is 50 ms +/- 5 ms including the ~ 1 cm flame radius extending beyond the flame centerline. This corresponds to a dwell-time in the centerline of ~40 ms, in-line with established flame sampling studies [14,27,28]. A small contribution of the TEM sample may be from particles captured away from the flame centerline in the relatively short transit time. Particles captured away the flame centerline are expected to grow under the same radially uniform temperature and species profiles [26,29,30], thus reducing contamination effects due to sampling position.

Carbon particle film deposition is also carried out on aluminum substrates mounted to the water cooled stagnation surface (Fig. 2c). The aluminum substrate is attached by a clamp having a tapered window exposing the substrate to the flame. A type K thermocouple is placed on the backside of the substrate with a measured wall temperature of $T_{stagnation}$ = 400 K. The aerosol dilution probe sampling process has also been described previously for similar premixed stagnation flames [11]. Aerosol dilution probe deposition (Fig. 2a) is carried out by mounting a

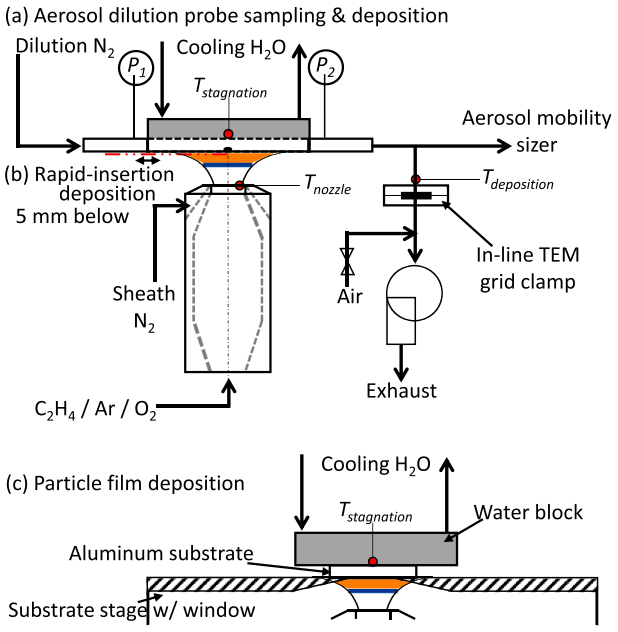

Fig. 2. Experimental schematic highlighting particle sampling methods used to deposit flame-formed carbon from the premixed stagnation flames. Aerosol dilution probe sampling followed by aerosol deposition onto a TEM grid (a), rapid-insertion deposition 5 mm below the stagnation plate (b) and particle film deposition onto an aluminum substrate (c). Red dots indicate type K thermocouple locations.

TEM grid in an in-line filter clamp exposing the grid to the diluted aerosol entering the vacuum pump. An in-line type K thermocouple is place immediately upstream of the filter clamp giving a measured gas temperature of $T_{deposition}$ = 375 K. HRTEM imaging is carried out for carbon samples collected from each of the above sampling methods on a Thermofisher Talos F200X at 200 keV acceleration voltage.

Particle film deposition on the stagnation surface enables more sample mass to be collected than deposition by rapid-insertion or from a diluted aerosol stream. Thus, off-line analysis by Raman spectroscopy and XPS is carried out using carbon particle films and not the other sampling methods. Raman spectra are obtained from the films as-deposited using a Renishaw inVia upright Raman microscope. Spectra from two excitation wavelengths (532 nm and 785 nm laser sources) are obtained to observe potential dispersion effects known to exist in graphenic materials. The carbon particle film is scraped and drop casted onto a nickel foil for XPS spectroscopy using a PHI 5600 with a A1 Kα light source. The carbon sample film is sputtered with argon ions in the vacuum chamber to prepare the sample surface for XPS analysis. Aerosol particle size distribution is also measured using a TSI 3838E77 SMPS with aerosol dilution probe methods introduced previously [11].

Results and discussion

TEM samples are collected by rapid insertion at a sampling height that is 0.5 cm below the stagnation surface. HRTEM images of flame-formed carbon collected by this method are shown in Fig. 3 for the two flame conditions. Qualitatively, the smaller particle size of the lighter sooting flame condition is expected but the observation of fractal like agglomerates in both flame conditions is an artificial deposition process. The HRTEM images reported are for a 50 ms insertion time but the supplementary material also includes results from a single 30 ms insertion. An optimal insertion time resulting in sufficient particle coverage without agglomerates was not found. The flame calculations summarized in Table 1 predict that the time a particle would travel between the flame zone and the stagnation boundary is on the order of

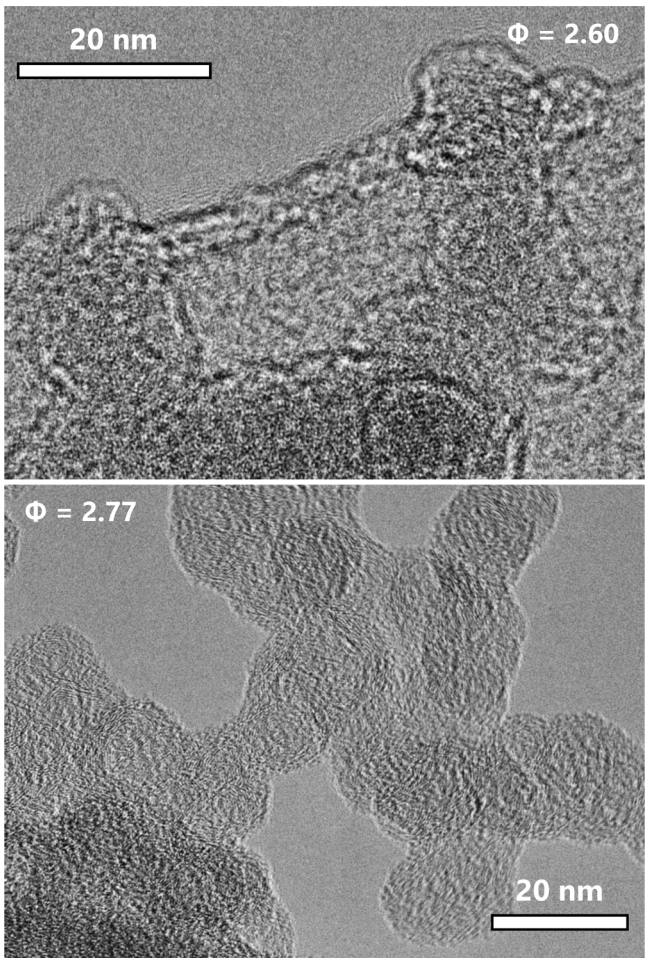

Fig. 3. HRTEM images of flame-formed carbon collected by rapid-insertion for the light sooting flame condition (Φ = 2.60, top) and heavy sooting flame condition (Φ = 2.77, bottom).

10 ms; a timescale in which only primary particles are expected. The observation of agglomerates on the TEM grid is an indication that agglomeration occurs upon exposure to particles and precursors during the rapid-insertion dwelling time. In terms of the particle lattice, a striking contrast is observed in which the higher equivalence ratio condition forms a well-defined turbostratic carbon lattice. Raman spectra previously reported for carbon formed under similar flame conditions [12] exhibited Raman peaks corresponding to graphenic materials but the morphology observed in Fig. 3 resembles amorphous carbon and soot nanostructure. The previous Raman spectra were measured from a carbon particle film grown at the stagnation surface over time. The current rapid insertion TEM samples could possibly lack graphenic nanostructure due to the shorter sample dwelling time and lower sampling position in the flame.

In addition to the flame formed carbon shown in Fig. 3, notable graphite nanocrystals, shown in Fig. 4, are also observed in rapid-insertion samples for both flame conditions. To the authors' knowledge, the formation of graphite nanocrystals has not been reported in flame deposition studies. Polyhedral graphite nanocrystals are observed (Fig. 4a) with lattice spacing of 0.34 nm corresponding to graphite. The width of the graphite nanocrystal is on the order of 50 nm which is too large for these particles to form in the flame by gas-to-particle conversion within the 10 ms residence time. The unique high-temperature, high-equivalence ratio environment of premixed stagnation flames may be inclined to artificial crystallization of abundant precursors. Rapid insertion and retraction of the cold TEM grid may enable artificial condensation and crystallization on the surface.

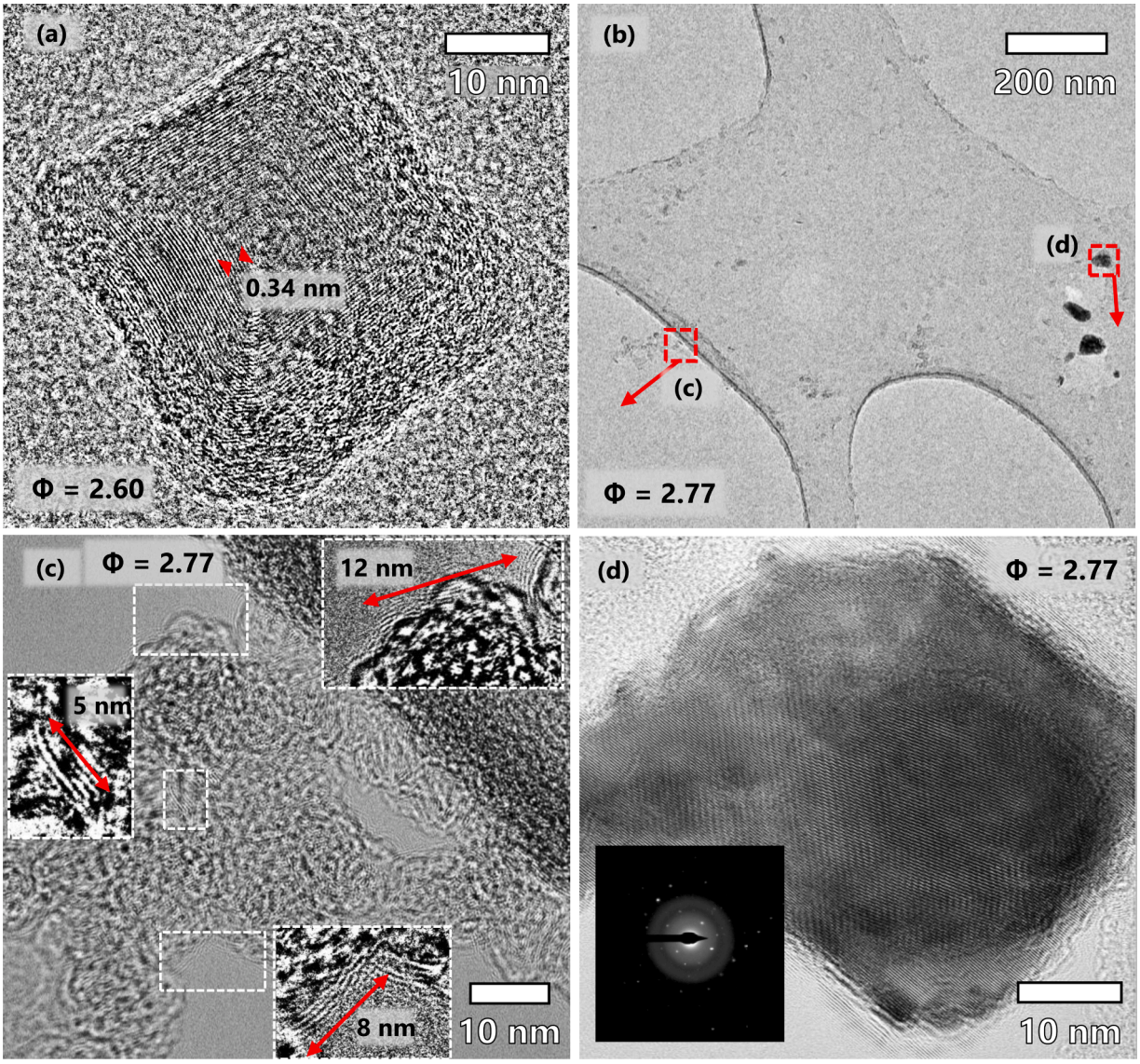

Fig. 4. HRTEM images of flame-formed carbon collected by rapid-insertion. Polyhedral graphite (a), low-magnification showing soot-like and graphite nano-crystal deposits (b) and high-magnification images of a soot-like nanoparticle region (c) and graphite region (d) with electron diffraction (d, inset).

Nanocrystals in a variety of shapes and structures (shown in Fig. S2) are observed. Further systematic work is required to determine the formation mechanism of these nanocrystals and the extent to which the lacey carbon (possible feedstock) and copper (possible catalyst) TEM substrates participate. Though not observed in all instances, some graphite nanocrystals are positioned at the edge of a discoloration (see e.g. Fig. 4b and d) which may indicate consumption / rupturing in the lacey carbon or pre-existing contamination. Fresh, unused TEM grids were examined to verify that the unexpected graphite nanocrystals are not present before the flame deposition experiments. The soot-like deposits (Fig. 4c) collected by rapid-insertion show an overall turbostratic structure but sections of longer lattice lengths can be found. Qualitive labels are provided to highlight unusually long lattice lengths observed in the soot-like particles. The current rapid-insertion samples show carbon nanomaterials in a wide range of nanostructures along with sampling artifacts that have not been reported before.

Dilution probe aerosol sampling is also used to characterize the flame-formed carbon. The mobility size distribution measured from the dilution probe is shown in Fig. 5 for both flame conditions. The aerosol distribution has a median mobility diameter of 6 nm and 12 nm for the low and high-sooting flame condition, respectively. This size scale indicates that the aerosol consists of primary particles at the smallest nanoparticle scale. A TEM sample is also collected by depositing from the aerosol flow onto a TEM grid clamped downstream of the dilution probe. Images of the deposited aerosol are shown in Fig. 6 for both flame conditions. Single primary particles are observed which corroborates the size scale of the measured mobility size distributions. Aspherical shapes are present, even in the smallest particles observed. Primary particles observed by TEM have been reported to deviate from spheres due to physical impact and “liquid-like” properties of incipient soot [13,31]. Larger, aspherical particles are also observed which may indicate artificial agglomeration on the substrate over the sample collection time. For rapid-insertion, the high precursor concentrations may induce condensation growth and agglomeration on the cold TEM grid, even in the fast immersion time-scale. Artificial condensation growth may also be occurring during the 5 min deposition time in which the diluted aerosol sample is collected. Further work is needed to obtain a greater sample size and to assess potential uncertainties in size distributions measured by TEM in this unique flame condition. The current experiment is successful at confirming the potential for depositing graphenic carbon but investigation of an optimal sample deposition time would allow for primary particles and small aggregates to be quantified

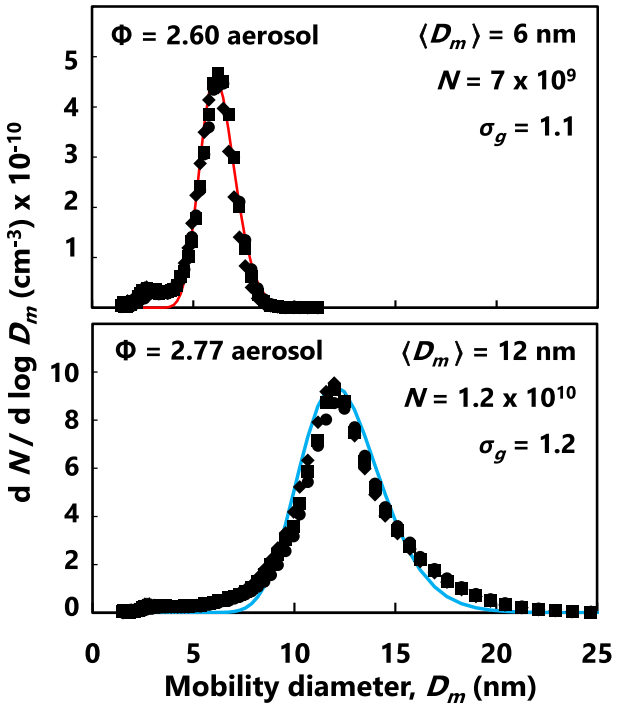

Fig. 5. Mobility size distribution of flame-formed carbon in the light sooting flame condition (Φ = 2.60, top) and heavy sooting flame condition (Φ = 2.77, bottom) measured by aerosol dilution probe sampling. The measurement is repeated 3 times, each measurement denoted by diamond, square or round symbols.

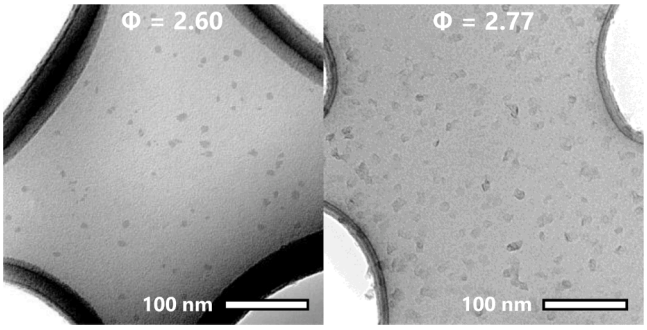

Fig. 6. Low-magnification TEM images of flame-formed carbon deposited downstream of the dilution probe for the light sooting flame condition (Φ = 2.60, left) and heavy sooting flame condition (Φ = 2.77, right).

without artificial condensation or kinetic growth.

Larger agglomerates are also observed on the aerosol deposition sample as shown in Fig. 7. The agglomerates are amorphous structures that presumably form by condensation of PAH over time. The aerosol flow is diluted by 1000x but the 5 min deposition time enables significant accumulation of carbon deposits. Interestingly, graphenic carbon structures are also embedded (Fig. 7c) within the amorphous agglomerates. The contrast enhanced inset shows clear graphene layers with 0.34 nm lattice spacing and length up to 12 nm. The gas temperature immediately upstream of the TEM grid is $T_{deposition}$ = 375 K as determined by an in-line type K thermocouple. This temperature is too low to expect significant chemical kinetic growth which may imply that the graphenic structures are formed in the flame or formed by probe sampling artifacts. The measured temperature at the stagnation plate of $T_{stagnation}$ = 400 K may only represent the sampling orifice wall and the

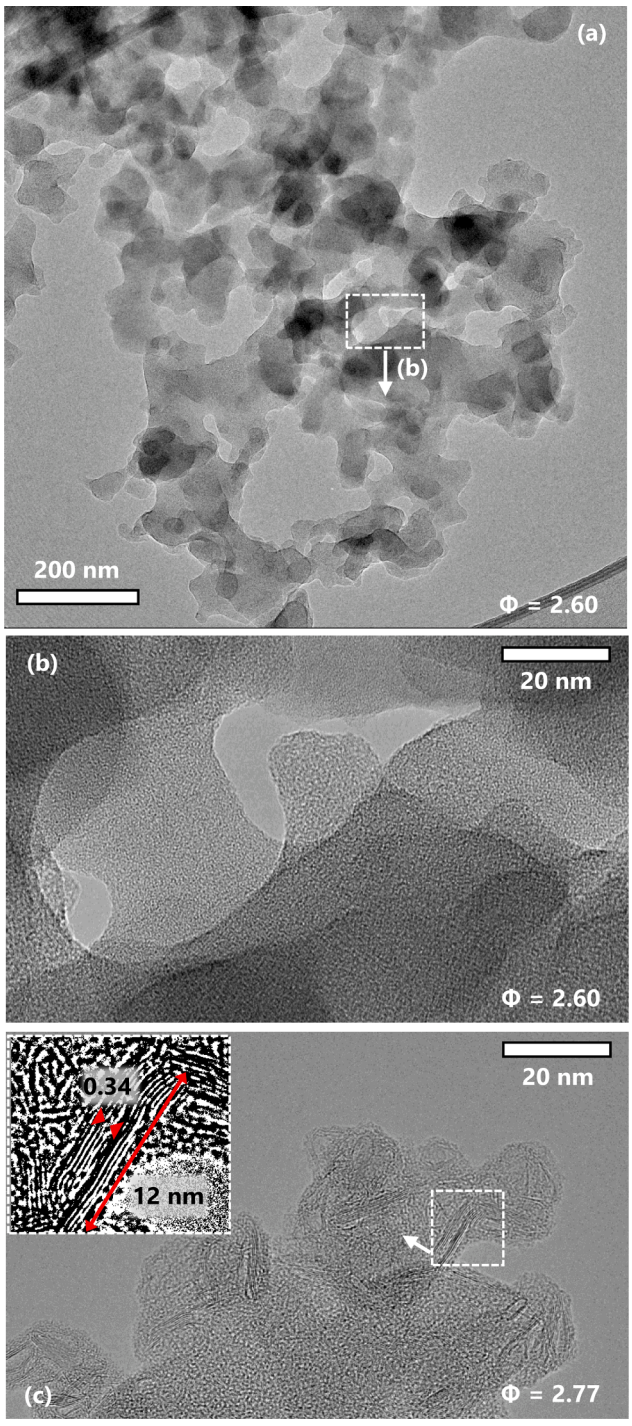

Fig. 7. HRTEM images of flame-formed carbon deposited downstream of the dilution probe. A large amorphous agglomerate in low-magnification (a) and high-magnification (b) and graphenic structures (c) along with a contrast-enhance section (c, inset).

aerosol volume entering the sampling orifice may be hot enough to prevent immediate quenching of kinetic growth processes.

Additional examples of carbon deposited from the diluted aerosol flow are shown in Figs. 8 and S3. The lower sooting flame condition is largely amorphous whereas the higher sooting flame condition shows more obvious graphene structures. The low magnification image (Fig. 8c) demonstrates conspicuous features markedly different than soot. More systematic sampling of the diluted aerosol with shorter deposition times is needed to gain a more rigorous relationship between

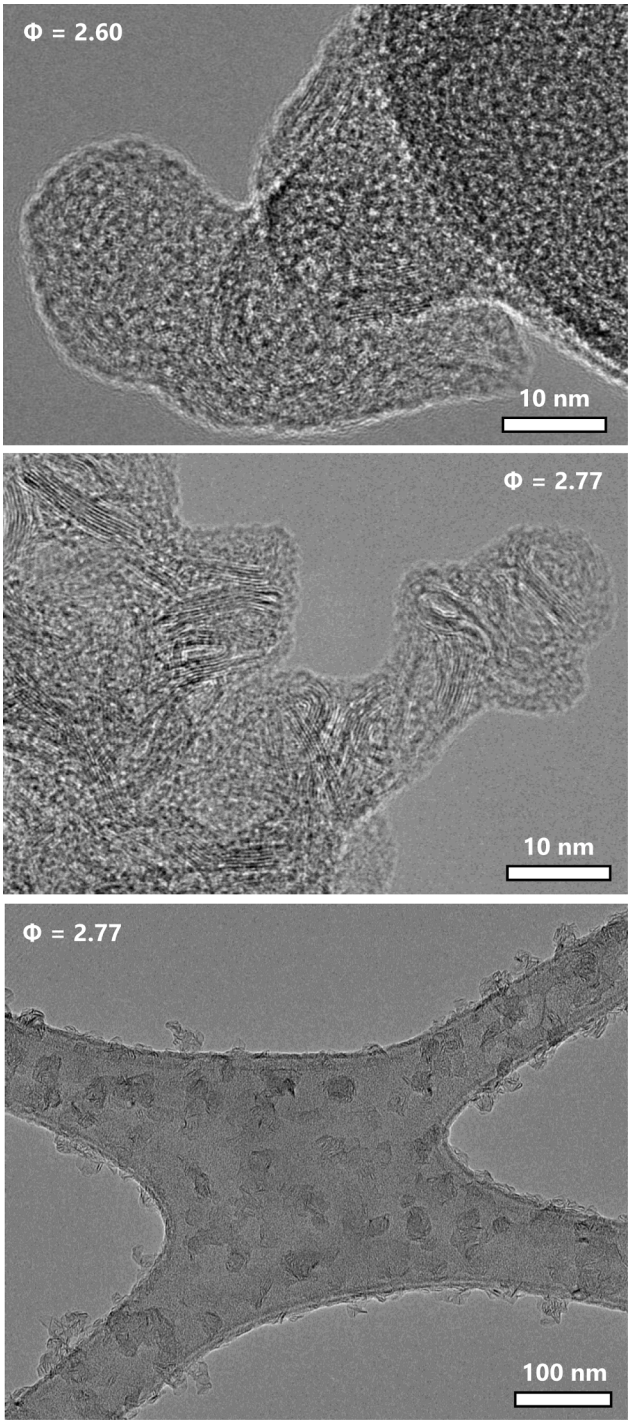

Fig. 8. HRTEM images of flame-formed carbon deposited downstream of the dilution probe. A typical deposit from the light sooting flame condition (Φ = 2.60, top), heavy sooting flame condition (Φ = 2.77, middle) and low-magnification image of the heavy sooting flame condition (Φ = 2.77, bottom).

the carbon particles formed in the flame and the deposition products observed on the TEM grid. Schulz and co-workers have reported [9,10] a competition between soot-like products and few-layer graphene in plasma synthesis based on oxygen concentration and an optimal carbon content of precursors. Investigation of ethanol fuel in future premixed stagnation flame studies may improve the yield of graphene products based on the previously reported impact of oxygen [9] towards favoring graphene over soot.

Carbon particle films deposited on the water-cooled stagnation surface are also characterized here. As shown in Fig. 1, the deposited carbon film accumulates significant mass over time and this facilitates off-line analysis by Raman spectroscopy and XPS. Raman spectra of primary peaks for the as-deposited carbon films are shown in Fig. 9 for both flames. Off-the-shelf hard carbon powder (MSE Supplies, 8 – 12 μm size) is also examined for comparison to a known disordered graphitic material. The 5-band deconvolution approach for carbon materials introduced by Sadezky and co-workers [32] is employed here. The position of the three major Raman peaks in the primary spectra is marked to highlight relative intensities and the response of the Raman shift to increasing excitation energy. A perfect graphite lattice should only exhibit the G-peak centered at 1580 cm^{-1} with minimal dispersion in wavenumber as excitation energy increases [33]. The D and D' peaks are due to aromatic sp^2 bonds and are commonly observed in defective graphite and other carbon materials. The intensity ratio of the D-peak to G-peak, I_D/I_G, has been used in semi-empirical analysis to quantify the relative area of graphenic sp^2 surface [34–36]. The $I_D/I_G > 1$ for the deposited carbon particle films and the relatively narrow peaks are characteristic of disordered graphite and graphenic materials. The broad peaks and $I_D/I_G \sim 1$ for the hard carbon powder are closer to the Raman spectrum of soot than graphenic materials. The D and D' wavenumber is

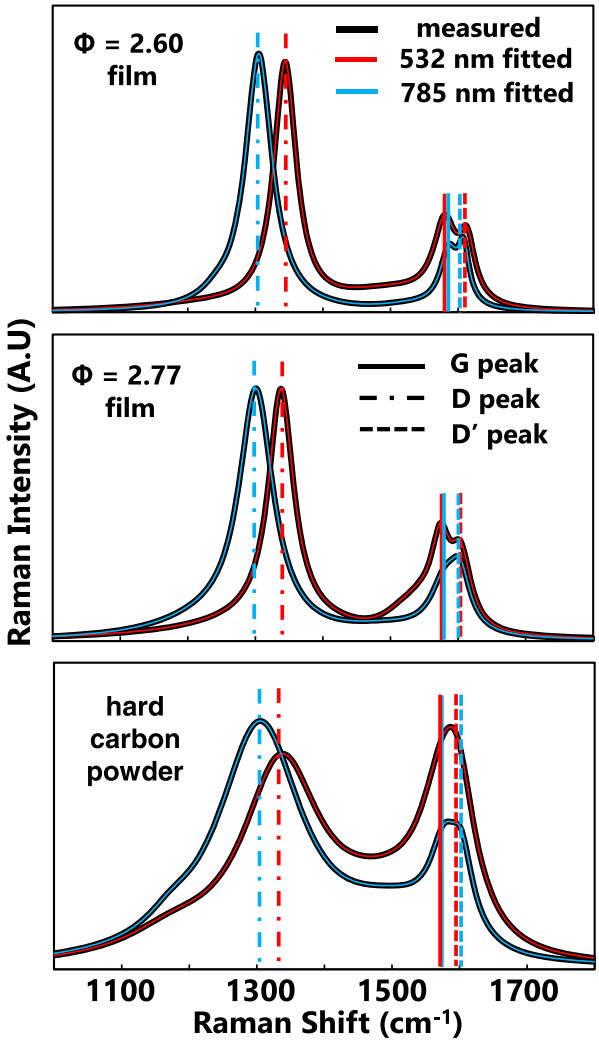

Fig. 9. Raman spectra (primary peaks) measured from carbon particle films deposited on the water cooled stagnation surface. Light sooting flame condition (Φ = 2.60, top), heavy sooting flame condition (Φ = 2.77, middle) and off-the-shelf hard carbon particles (bottom).

known to shift with increasing excitation energy by 50 cm^{-1} / eV and 10 cm^{-1} / eV, respectively [35]. This behavior is indeed observed for these peaks at the current excitation energies of 1.58 eV (785 nm) and 2.33 eV (532 nm).

Analysis of the secondary Raman peaks provides additional insights into the carbon structure of the deposited carbon particle films. The Raman spectra of secondary peaks with marked peak positions is shown in Fig. 10. The primary peak spectra shows subtle differences between the two flame conditions whereas the secondary peak spectra have more distinct differences. The 2D peak is an overtone of the D peak with known dispersion on the order of 100 cm^{-1} / eV in graphenic materials [37]. The $D + D''$ peak is known to have a red shift with increasing excitation energy. Both of these responses are observed in the $\Phi = 2.60$ condition whereas the $D + D''$ becomes undetectable in the $\Phi = 2.77$ case under 2.88 eV (532 nm) excitation. The relative intensity and dispersion of the $D + D'$ peak is similar for both flame conditions but the absolute intensities are different across all of the secondary peaks considered. The observed secondary Raman spectra and dispersion behavior is consistent with disordered graphite and graphenic materials but there are quantitative differences between the two flame conditions. The secondary spectra for the hard carbon material exhibits different features than expected for graphenic materials. The $D + D'$ is the most intense secondary peak under the 2.88 eV (532 nm) energy and the hard carbon spectrum shifts into a spectrum inconsistent with graphene under 1.33 eV (785 nm). Raman spectra for carbon particle films deposited on the water-cooled stagnation surface have clear indications that graphenic carbon structures are present but the film may not represent properties of the carbon in the flame.

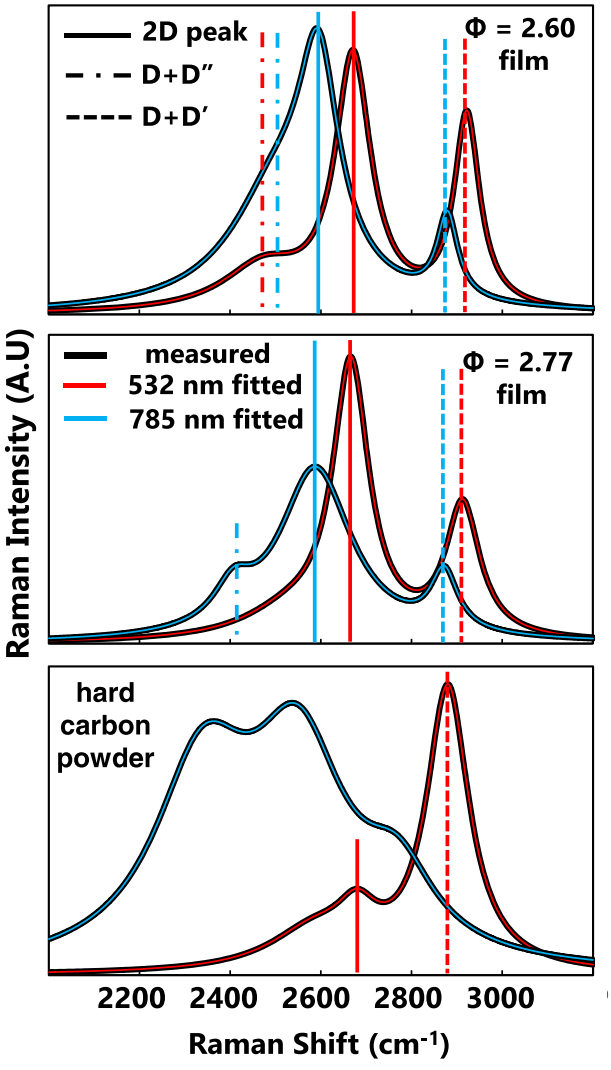

Fig. 10. Raman spectra (secondary peaks) measured from carbon particle films deposited on the water cooled stagnation surface. Light sooting flame condition ($\Phi = 2.60$, top), heavy sooting flame condition ($\Phi = 2.77$, middle) and off-the-shelf hard carbon particles (bottom).

The carbon particle film deposited on the water-cooled surface is also used to prepare a TEM sample by scraping the film, dispersing by sonication in THF solvent and drop-casting onto the grid. The TEM sample preparation method is adapted from the ASTM standard for HRTEM of carbon black materials [38]. HRTEM images of particles in the deposited film are shown in Figs. 11 and S4 for both flame conditions. The carbon particle film deposit shows the most the distinguishable graphenic features compared to the other sampling methods. For the film under the light sooting flame condition (Fig. 11a), individual flakes can be observed with approximately 2 dozen graphene layers. It is difficult to avoid clustering of individual particles for drop-casted TEM samples but, nonetheless, the extensive amount of graphenic structure is obvious for both flame conditions.

The film growth is a particle deposition process in which flame-formed carbon particles approach the stagnation surface and build a porous film within the plate boundary layer. A dark carbon film is grown within a 5 min deposition time for the heavier sooting flame condition. In contrast, the light sooting flame takes 40 min to deposit an appreciable film (see Fig. 1b) due to the lower particle concentration and smaller particle sizes. The temperature at the back-side of the deposition substrate is measured as $T_{stagnation} = 400$ K by a thermocouple embedded flush with the surface. If the thermal conductivity of the porous film is low, then it is possible that the flame facing film surface is hot enough to undergo kinetic growth processes as abundant carbon precursors flow over the film. In a relatively simple scenario, the heat transfer across the porous film could be calculated given the effective thermal conductivity of the carbon or average across amorphous, soot and graphene contributions. An additional complexity is the abundant gas-phase precursors constantly feeding into the porous film which may alter the thermal transport of the porous film in a non-trivial way. Surface adsorption and/or condensation of oily hydrocarbons may introduce thermal insulation which could increase the local film temperature. The drop-casted particles are graphenic for both flame conditions which may indicate that kinetic growth processes occur in both films as they are effectively cut-off from the plate water-cooling on the flame facing surface. Even within 5 min, the particle film is much thicker for the heavier sooting flame condition (see Fig. 1c). This condition has a much higher concentration of gas-phase precursors and the thicker film may lead to an even hotter temperature on the flame facing surface.

The carbon particle film is also drop-casted onto a nickel foil for XPS analysis. XPS spectra at the C1s binding energy are shown in Fig. 12 for the two flame conditions and hard carbon powder. The peak is deconvoluted using CasaXPS software (v. 2.3.24) into background corrected sp^2 and sp^3 peaks using a Shirley background correction and Lorentzian axisymmetric lineshapes. The ratio of areas of the deconvoluted sp^2 and sp^3 peaks is assumed to correspond to the proportion of sp^2 and sp^3 bonding at the sample surface [39]. This analysis results in 47%, 62% and 75% sp^2 bonding for the hard carbon, $\Phi = 2.60$ and $\Phi = 2.77$ condition, respectively. The balance is assumed to be sp^3 bonded. The HRTEM images of the drop-casted samples show graphenic structures in both flame conditions but the higher sp^2 content measured in the higher sooting flame condition is consistent the rapid-insertion and aerosol deposition TEM samples.

Although the contributions of flame-formed carbon versus artificial deposition processes have not been quantified, the above observations clearly highlight the unique high-temperature, high-equivalence ratio environment of premixed stagnation flames. The rapid-insertion method has the greatest potential to the capture carbon samples with properties frozen as they were in the flame. However, the current rapid-insertion

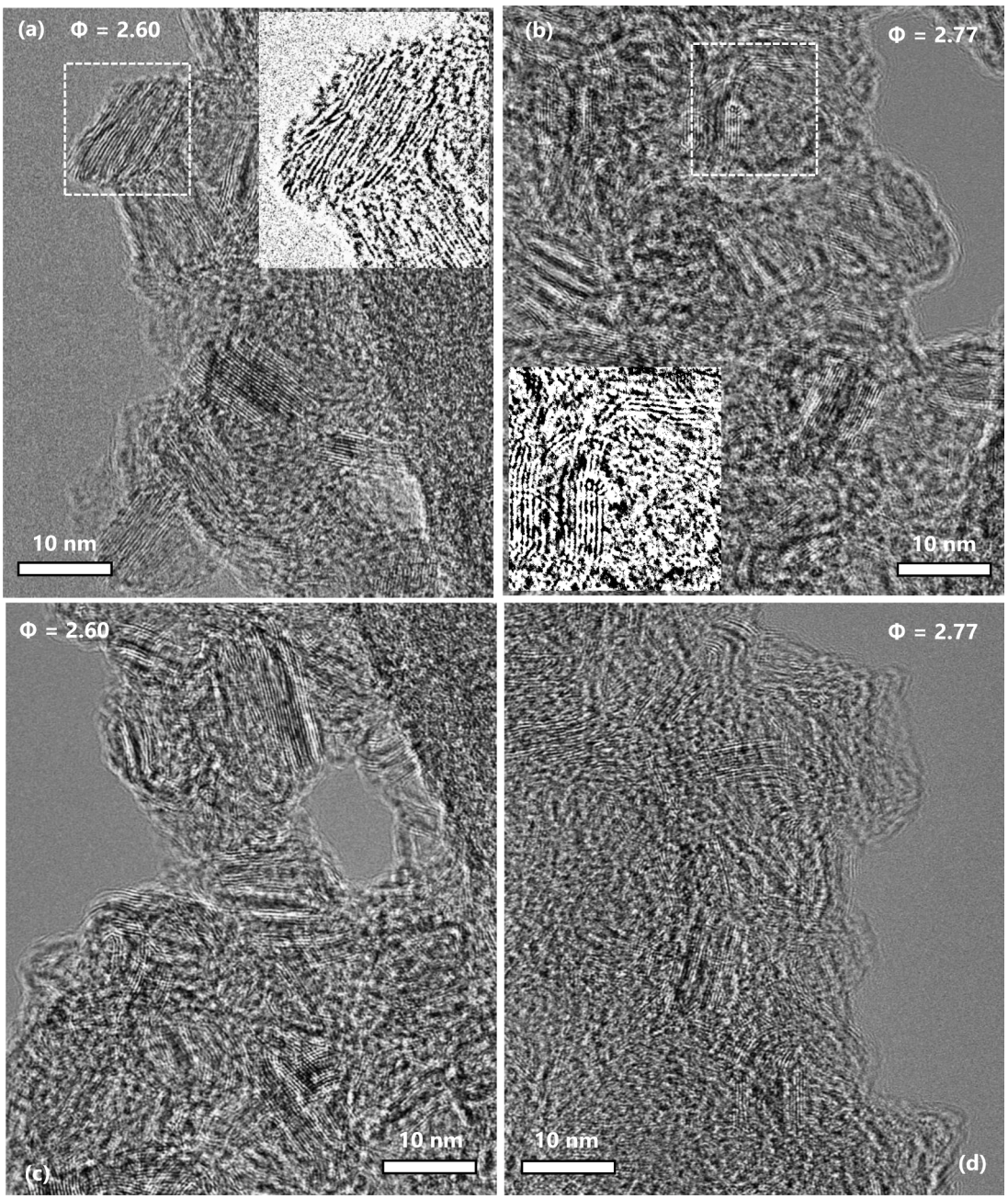

Fig. 11. HRTEM images of particles collected from the carbon particle film grown on the water-cooled stagnation surface. Light sooting flame condition (Φ = 2.60, a, c), heavy sooting flame condition (Φ = 2.77, b, d) with contrast-enhanced portions (insets).

samples were captured 0.5 cm from the stagnation boundary and the grid was exposed to the substantial secondary flame burning excess hydrocarbons around the main flame. A new rapid-insertion device is being designed for future sampling at the stagnation surface boundary with exposure only to the centerline of the main flame. Systematic studies to elucidate the formation mechanism of the reported graphite nanocrystal artifacts are also underway. Deposition from the aerosol dilution probe flow is also promising but the dilution should be maximized and the deposition time should be minimized to ensure the deposited particles closely represent the carbon nanoparticles in the flame.

Conclusion

Premixed stretch-stabilized flames enable graphenic carbon particle production in excessively high flame temperature in a relatively simply flow field. However, the current work highlights the importance of careful interpretation of particle properties derived from intrusive sampling techniques. Potential sampling artifacts are commonly discussed, even for simple laboratory flames, but, the current high-temperature, high-equivalence ratio environment introduces new processes such as artificial crystallization and, potentially, kinetic growth processes during deposition.

The current measurements indicate that graphenic materials could be forming in the flame, but new measurements optimized for the unique flame environment are required to pin down the proper boundary conditions and eliminate artifacts. Overall, the carbon nanostructure observed by HRTEM is a mixture of amorphous, turbostratic and graphenic carbon lattices depending on the flame condition and sampling method. HRTEM of particles deposited over time and

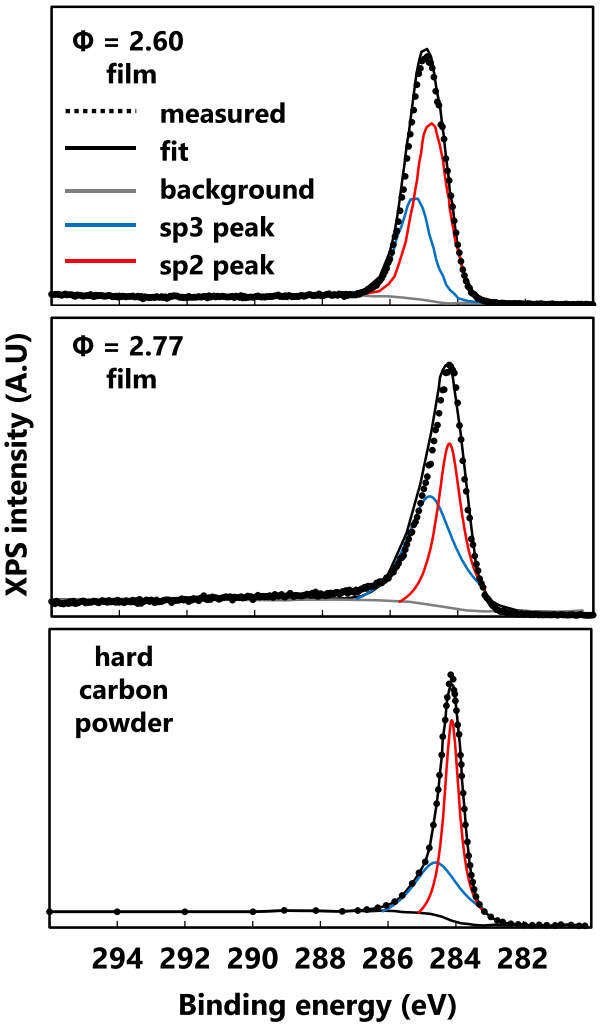

Fig. 12. XPS spectra measured from drop-casted samples of carbon particle films deposited on the water cooled stagnation surface. Light sooting flame condition (Φ = 2.60, top), heavy sooting flame condition (Φ = 2.77, middle) and off-the-shelf hard carbon particles (bottom).

corresponding Raman and XPS analysis show clear graphenic particle properties. However, quantifying the contributions of flame-based and deposition processes in this high-temperature, high-equivalence ratio environment requires further study.

The current work corroborates previous observations [12] that sootier flames produce carbon with more graphenic properties. In future work, even sootier flames may reduce the experimental challenges reported here by increasing the yield of graphenic materials which would reduce the sample collection time required to obtain a measurable sample. Maintaining higher flame temperatures for higher equivalence ratio can be achieved by lowering the argon concentration and increasing the cold gas velocity. The sample collection time reduction is most beneficial but the increase in excess fuel will further increase interference by gas-phase precursors. Less sooty flames produce smaller particles but the small particle size and lower yield makes fundamental investigations and systematic characterization much more challenging.

Declaration of Competing Interest

The authors declare that they have no known competing financial interests or personal relationships that could have appeared to influence the work reported in this paper.

Data availability

Data will be made available on request.

Acknowledgments

This work is supported by US National Science Foundation Award 2143979. This work was performed in part at the San Diego Nanotechnology Infrastructure (SDNI) of UCSD, a member of the National Nanotechnology Coordinated Infrastructure, which is supported by the National Science Foundation (ECCS-2025752).

Supplementary materials

Supplementary material associated with this article can be found, in the online version, at doi:10.1016/j.jaecs.2023.100178.

References

[1] Heywood JB. Internal combustion engine fundamentals. New York: McGraw-Hill; 2018.
[2] Radney JG, You R, Ma X, Conny JM, Zachariah MR, Hodges JT, Zangmeister CD. Dependence of soot optical properties on particle morphology: measurements and model comparisons. Environ Sci Technol 2014;48:3169–76. https://doi.org/10.1021/es4041804.
[3] Ulrich GD. Special report: flame-generated fine particles. Chem Eng New Arch 1984;62:22–9. https://doi.org/10.1021/cen-v062n032.p022.
[4] Donnet J-B, Bansal RC, Wang M-J. Carbon black. New York: Marcel Dekker; 1993.
[5] Howard JB. Fullerenes formation in flames. In: Symposium (International) on Combustion. 24; 1992. p. 933–46. https://doi.org/10.1016/S0082-0784(06)80111-6.
[6] Bachmann M, Wiese W, Homann K-H. PAH and aromers: precursors of fullerenes and soot. In: Symposium (International) on Combustion. 26; 1996. p. 2259–67. https://doi.org/10.1016/S0082-0784(96)80053-1.
[7] Li S, Ren Y, Biswas P, Tse SD. Flame aerosol synthesis of nanostructured materials and functional devices: processing, modeling, and diagnostics. Prog Energy Combust Sci 2016;55:1–59. https://doi.org/10.1016/j.pecs.2016.04.002.
[8] Memon NK, Xu F, Sun G, Dunham SJB, Kear BH, Tse SD. Flame synthesis of carbon nanotubes and few-layer graphene on metal-oxide spinel powders. Carbon N Y 2013;63:478–86. https://doi.org/10.1016/j.carbon.2013.07.023.
[9] Fortugno P, Musikhin S, Shi X, Wang H, Wiggers H, Schulz C. Synthesis of freestanding few-layer graphene in microwave plasma: the role of oxygen. Carbon N Y 2022;186:560–73. https://doi.org/10.1016/j.carbon.2021.10.047.
[10] López-Cámara C-F, Fortugno P, Asif M, Musikhin S, Prindler C, Wiggers H, Endres T, Eaves N, Daun KJ, Schulz C. Evolution of particle size and morphology in plasma synthesis of few-layer graphene and soot. Combust Flame 2023:112713. https://doi.org/10.1016/j.combustflame.2023.112713.
[11] Bonpua J, Yagües Y, Aleshin A, Dasappa S, Camacho J. Flame temperature effect on sp2 bonds on nascent carbon nanoparticles formed in premixed flames (T > 2100 K): a Raman spectroscopy and particle mobility sizing study. Proc. Combust. Inst. 2019;37:943–51. https://doi.org/10.1016/j.proci.2018.06.124.
[12] Dasappa S, Camacho J. Evolution in size and structural order for incipient soot formed at flame temperatures greater than 2100 Kelvin. Fuel 2021;291:120196.
[13] Kholghy M, Saffaripour M, Yip C, Thomson MJ. The evolution of soot morphology in a laminar coflow diffusion flame of a surrogate for Jet A-1. Combust Flame 2013;160:2119–30. https://doi.org/10.1016/j.combustflame.2013.04.008.
[14] Botero ML, Akroyd J, Chen D, Kraft M, Agudelo JR. On the thermophoretic sampling and TEM-based characterisation of soot particles in flames. Carbon N Y 2021;171:711–22. https://doi.org/10.1016/j.carbon.2020.09.074.
[15] Chadha TS, Yang M, Haddad K, Shah VB, Li S, Biswas P. Model based prediction of nanostructured thin film morphology in an aerosol chemical vapor deposition process. Chem Eng J 2017;310:102–13. https://doi.org/10.1016/j.cej.2016.10.105. Part.
[16] Zhao B, Yang Z, Wang J, Johnston MV, Wang H. Analysis of soot nanoparticles in a laminar premixed ethylene flame by scanning mobility particle sizer. Aerosol Sci Technol 2003;37:611–20. https://doi.org/10.1080/02786820300908.
[17] Carbone F, Attoui M, Gomez A. Challenges of measuring nascent soot in flames as evidenced by high-resolution differential mobility analysis. Aerosol Sci Technol 2016;50:740–57. https://doi.org/10.1080/02786826.2016.1179715.
[18] Law CK. Combustion physics. Cambridge: Cambrige Press; 2006.
[19] Dasappa S. PhD Thesis. UC San Diego; 2021.
[20] Frenklach M, Taki S, Durgaprasad MB, Matula RA. Soot formation in shock-tube pyrolysis of acetylene, allene, and 1,3-butadiene. Combust Flame 1983;54:81–101. https://doi.org/10.1016/0010-2180(83)90024-X.
[21] Abid AD, Heinz N, Tolmachoff ED, Phares DJ, Campbell CS, Wang H. On evolution of particle size distribution functions of incipient soot in premixed ethylene–oxygen–argon flames. Combust Flame 2008;154:775–88. https://doi.org/10.1016/j.combustflame.2008.06.009.

[22] R.J. Kee, F.M. Rupley, J.A. Miller, Chemkin-II: a Fortran chemical kinetics package for the analysis of gas-phase chemical kinetics, (1989).
[23] A.E. Lutz, R.J. Kee, J.F. Grcar, F.M. Rupley, OPPDIF: a Fortan program for computing opposed-flow diffusion flames, (1997).
[24] Abid AD, Camacho J, Sheen DA, Wang H. Quantitative measurement of soot particle size distribution in premixed flames - The burner-stabilized stagnation flame approach. Combust Flame 2009;156:1862–70.
[25] H. Wang, X. You, A.V. Joshi, S.G. Davis, A. Laskin, F. Egolfopoulos, C.K. Law, USC Mech II. High-Temperature Combustion Reaction Model of H2/CO/C1-C4 Compounds, https://Ignis.Usc.Edu/USC_Mech_II.Htm. (2007).
[26] Dasappa S, Camacho J. Formation of nanocrystalline manganese oxide in flames: oxide phase governed by classical nucleation and size-dependent equilibria. CrystEngComm 2020;22:5509–21. https://doi.org/10.1039/D0CE00734J.
[27] Dobbins RA, Megaridis CM. Morphology of flame-generated soot as determined by thermophoretic sampling. Langmuir 1987;3:254–9. https://doi.org/10.1021/la00074a019.
[28] Vander Wal RL, Tomasek AJ. Soot nanostructure: dependence upon synthesis conditions. Combust Flame 2004;136:129–40. https://doi.org/10.1016/j.combustflame.2003.09.008.
[29] Seshadri K, Williams FA. Laminar flow between parallel plates with injection of a reactant at high reynolds number. Int J Heat Mass Transf 1978;21:251–3. https://doi.org/10.1016/0017-9310(78)90230-2.
[30] Meeks E, Kee RJ, Dandy DS, Coltrin ME. Computational simulation of diamond chemical vapor deposition in premixed C2H2/O2/H2 and CH4O2-strained flames. Combust Flame 1993;92:144–60. https://doi.org/10.1016/0010-2180(93)90204-G.
[31] Zhao B, Uchikawa K, Wang H. A comparative study of nanoparticles in premixed flames by scanning mobility particle sizer, small angle neutron scattering, and transmission electron microscopy. Proc. Combust. Inst. 2007;31:851–60. https://doi.org/10.1016/j.proci.2006.08.064.
[32] Sadezky A, Muckenhuber H, Grothe H, Niessner R, Poschl U. Raman microspectroscopy of soot and related carbonaceous materials: spectral analysis and structural information. Carbon N Y 2005;43:1731–42. https://doi.org/10.1016/j.carbon.2005.02.018.
[33] Malard LM, Pimenta MA, Dresselhaus G, Dresselhaus MS. Raman spectroscopy in graphene. Phys Rep 2009;473:51–87. https://doi.org/10.1016/j.physrep.2009.02.003.
[34] Ferrari AC, Robertson J. Interpretation of Raman spectra of disordered and amorphous carbon. Phys Rev B 2000;61:14095–107.
[35] Ferrari AC, Basko DM. Raman spectroscopy as a versatile tool for studying the properties of graphene. Nat Nanotechnol 2013;8:235. https://doi.org/10.1038/nnano.2013.46. https://www.nature.com/articles/nnano.2013.46#supplementary-information.
[36] Cançado LG, Takai K, Enoki T, Endo M, Kim YA, Mizusaki H, Jorio A, Coelho LN, Magalhães-Paniago R, Pimenta MA. General equation for the determination of the crystallite size La of nanographite by Raman spectroscopy. Appl Phys Lett 2006;88:163106. https://doi.org/10.1063/1.2196057.
[37] Cançado LG, Jorio A, Ferreira EHM, Stavale F, Achete CA, Capaz RB, Moutinho MVO, Lombardo A, Kulmala TS, Ferrari AC. Quantifying defects in graphene via Raman spectroscopy at different excitation energies. Nano Lett 2011;11:3190–6. https://doi.org/10.1021/nl201432g.
[38] I.S. Organization, Standard Test Method For Carbon Black—Morphological Characterization Of Carbon Black Using Electron Microscopy, ASTM D3849 − 14a. (2014).
[39] Filik J, May PW, Pearce SRJ, Wild RK, Hallam KR. XPS and laser Raman analysis of hydrogenated amorphous carbon films. Diam Relat Mater 2003;12:974–8. https://doi.org/10.1016/S0925-9635(02)00374-6.